



Multi-dimensional Pt–Mo/Co@NC nanocomposites with low platinum contents for methanol oxidation

Jinxing Wang¹ · Jiahui Xu¹ · Zihe Chen¹ · Xianbao Wang¹

Received: 30 January 2022 / Revised: 11 October 2022 / Accepted: 11 October 2022 / Published online: 9 November 2022
© The Author(s), under exclusive licence to Springer-Verlag GmbH Germany, part of Springer Nature 2022

Abstract

The high cost, CO poisoning, and slow electro-oxidation kinetics of Pt-based noble metal catalysts limit the merchandizing of direct methanol fuel cell. Here, metal zeolite imidazole frameworks composites are used to acquire a small amount (6.5 wt%) of Pt nanoparticles modified molybdenum carbide-decorated metallic cobalt@nitrogen-doped carbon nanohybrid materials (Pt–Mo/Co@NC). Compared with the merchant Pt/C catalysts, the obtained Pt–Mo/Co@NC composites exhibit substantially enhanced electrocatalytic activity and stability, and the mass activity reaches 1727 mA mg⁻¹ at –0.1 V, which is about 4.3 times that of merchant Pt/C catalysts.

Keywords Anode catalysts · Methanol oxidation reaction · Low Pt loadings catalyst · Fuel cell

Introduction

The direct methanol fuel cell (DMFC) [1], as a portable fuel cell, has received widespread attention [2], and the methanol oxidation reaction (MOR) is the most critical step to enhance the energy conversion efficiency [3, 4]. It is found that both precious metals and transition metals show highly catalytic performance for MOR [5, 6]. Among them, the precious metal platinum (Pt) has the optimal catalytic performance [7], but the high cost and low utilization of platinum precious metal restrict the development of platinum-based catalysts [8]. In addition, the slow electrooxidation kinetics and CO intoxication of Pt electrocatalysts during MOR usually result in a rapid loss of electrocatalytic performance [9–11].

Therefore, developing low-cost alternative catalysts with high activity, high stability, as well as high durability is important for DMFC [12, 13]. At present, the platinum content of commercial platinum–carbon catalysts used in fuel cells is more than 20 wt%, but its catalytic activity and

utilization rate are not satisfactory. Numerous efforts have been devoted to overcome this major obstacle and accelerate the commercialization of DMFC [14–18]. On the one hand, platinum-based catalysts can be designed with a core–shell structure [19, 20] or a porous structure to decrease the platinum content by increasing the active sites [21]; on the other hand, according to the synergistic effect between multiple metals, platinum nanocrystals can be combined with transition metals to form multi-element alloy catalysts, which can improve the catalytic efficiency with reducing the platinum content [22–25]. In addition, non-precious metal catalysts can be explored to replace platinum-based catalysts, and according to the *d-band* center theory [26], for example, a series of transition metal oxides [27–30], sulfides [31, 32], and carbides [33] are used to explore non-noble metal catalysts in electrocatalysis applications [34]. The electronic structure of transition metal carbides is connected with the interaction between metal atoms and carbon [35–41]. Therefore, by inhibiting the agglomeration of the active phase during the carbonization process, more catalytic sites are exposed to enhance the catalytic efficiency of the carbide [42].

Due to immediate availability and better charge storage properties, numerous nanocomposites show important application prospects in the fields of photovoltaics, sensors, energy conversion, and energy storage [43, 44]. Chitosan with NaI was synthesized by Rahman et al. and applied as a solid polymer electrolyte for dye-sensitised solar cells to improve their

✉ Xianbao Wang
wangxb68@aliyun.com

¹ Ministry of Education Key Laboratory for the Green Preparation and Application of Functional Materials, Hubei Key Laboratory of Polymer Materials, Collaborative Innovation Center for Advanced Organic Chemical Materials Co-Constructed By the Province and Ministry, School of Materials Science and Engineering, Hubei University, Wuhan 430062, People's Republic of China

ionic conductivity [45]. Composite gel polymer electrolyte (CGPE) was used by Amici et al. to enhance lithium ion conductivity in safer Li-O₂ batteries [46]. Carbonized composite nanostructured silicon-sulfur composites were synthesized by Alidoost et al. and used to replace lithium metal anodes in sulfur batteries [47]. A laser-induced graphene (LIG) network captures and interconnects activated carbon (AC) particles and was used by Reina et al. to increase the electrical double-layer capacitance of LIG electrodes [48]. Polymanganese oxide was coated on the surface of porous carbon nanofibers by Abdah et al. to increase catalytic activity and buffer volume changes during cycling [49].

MOFs have a porous framework structure [50], which is a good functional material to prepare carbide composites [22]. MOFs were used as the key precursors [51] for low-cost and controlled synthesis of nano-structures [52]. Zeolitic imidazolate frameworks (ZIFs) [53] are considered to be one of the most suitable precursors [22, 54–57]. For example, ZIF-L [58] and ZIF-M-X [31] are metal-carbon hybrid precursors with large surface areas [54]. In addition, it is difficult for MOFs to be used directly as electrocatalysts because of its poor conductivity. In order to solve the disadvantage, several MOFs were designed to obtain high-performance electrocatalysts with good electrical conductivity and chemical stability through forming highly conductive carbon [59] and N-doped metal nanohybrids [60]. It is also possible to prepare carbon-supported metal oxides, phosphides, or metal nanoparticles through a special post-treatment process [59].

Here, through simple microwave-assisted reduction, a small amount of Pt nanoparticles was deposited on the surface of the Mo/Co@NC, and multi-dimensional Pt-Mo/Co@NC nanocomposites with low platinum content (6.5 wt%) are finally obtained to explore their application in methanol oxidation.

Experimental section

Reagents and materials

Cobaltous nitrate (Co(NO₃)₂·6H₂O), 2-methylimidazole (C₄H₆N₂), ammonium molybdate tetrahydrate ((NH₄)₆Mo₇O₂₄·4H₂O), polyvinylpyrrolidone (PVP), ethanol (C₂H₅OH), potassium hydroxide (KOH), methanol (CH₃OH), and ascorbic acid (AA) were purchased obtained Sinopharm Chemical Reagent Co., Ltd. (Shanghai, China). Nafion (5wt%) and K₂PtCl₄ were purchased from Sigma-Aldrich.

Catalyst preparation

Co-ZIF NPs

The Co-ZIF NPs were prepared based on the literature. Firstly, 4 mmol Co(NO₃)₂·6H₂O and 16 mmol PVP were

evenly dispersed in 20 mL methanol to form solution I and sonication for 10 min. Then, 8 mmol of 2-methyl imidazole was uniformly dispersed in 10 mL of methanol to obtain solution II. Then, the solution II was added to the solution I, and, after evenly stirring, the reaction was hydrothermally reacted at 120 °C for 2 h. Finally, the obtained products were centrifuged, washed, and dried.

Mo/Co-ZIF NPs

Firstly, 10 mg (NH₄)₆Mo₇O₂₄·4H₂O was uniformly dispersed in the aqueous solution to form solution A, and 100 mg of Co-ZIF was uniformly dispersed 20 ml of methanol to form solution B. Secondly, solution A was injected to B and evenly stirred for 2 h. Finally, Mo/Co-ZIF NPs were obtained after being dried at 60 °C for 12 h under vacuum.

Mo/Co@NC NPs

The as-prepared Mo/Co-ZIF precursor was pyrolyzed at 900 °C for 2 h in an N₂ atmosphere, and then Mo/Co@NC nanocomposite could be obtained. In addition, Co@NC nanocomposite materials could be obtained by the same method.

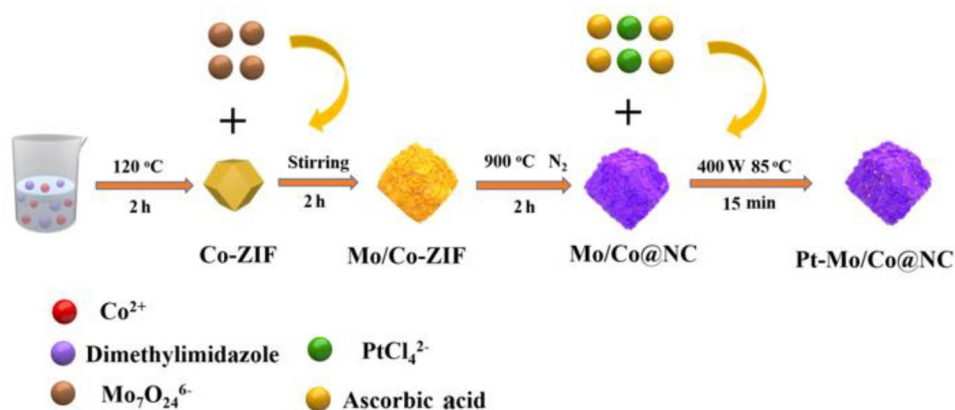
Pt-Mo/Co@NC NPs

A total of 20 mg of Mo/Co@NC was uniformly dispersed in 20 mL of deionized water, and then 50 mg of AA was added. After ultrasonic stirring, 10 mg of K₂PtCl₄ evenly dispersed in 5 ml of deionized water was added to the mixed solution, which then was irradiated by microwave (400 W) at 85 °C for 10 min. After centrifugal washing, the resulting black substance was freeze-dried to obtain the Pt-Mo/Co@NC. For comparison, the Pt-Co@NC nanocomposite materials could be obtained by the same method.

Physicochemical characterization

The surface structure and micromorphology of the as-prepared catalysts were analyzed by transmission electron microscopy (TEM) and HRTEM (Tecnai Talos, Netherlands). X-ray diffraction (XRD) was implemented using a D8-Advance diffractometer (Germany) with a Cu K α radiation source ($\beta = 0.15418$ nm). Element distribution was detected by energy-dispersive X-ray spectroscopy (EDX, JSM6510LV, Japan) and field emission scanning electron microscopy (FE-SEM, JSM7100F). The elemental composition of the as-prepared catalysts was analyzed through X-ray photoelectron spectroscopy (XPS; Thermo Fisher Scientific Escalab250Xi).

Scheme 1 The schematic illustration of the synthesis process of Pt–Mo/Co@NC



Electrochemical characterization

The CHI760E (Shanghai Chenhua, China) was used for electrochemical analysis at room temperature in a three-electrode configuration. A modified glass carbon electrode (GCE) (3 mm in diameter), a platinum electrode, and a saturated calomel electrode (SCE) were used as the work, counter, and reference electrodes, respectively. Each specimen was ultrasonically treated with 500 μL of ethanol to obtain a uniform catalyst ink of 2 mg mL^{-1} . After ultrasonic cleaning for 60 min, a 2 μL droplet of the resulting mixture was pressed onto the polished GCE and dried at 25 $^{\circ}\text{C}$ for 1 h. After ultrasonic cleaning for 60 min, a 2 μL catalyst ink was pressed onto the cleaned GCE and dried at room temperature. N_2 was blown into the electrolyte for 30 min to avoid the influence of air for the test results. The electrolyte solution for the methanol oxidation test consisted of 1.0 M KOH and 1.0 M CH_3OH .

Results and discussion

The synthesis method of Pt–Mo/Co@NC

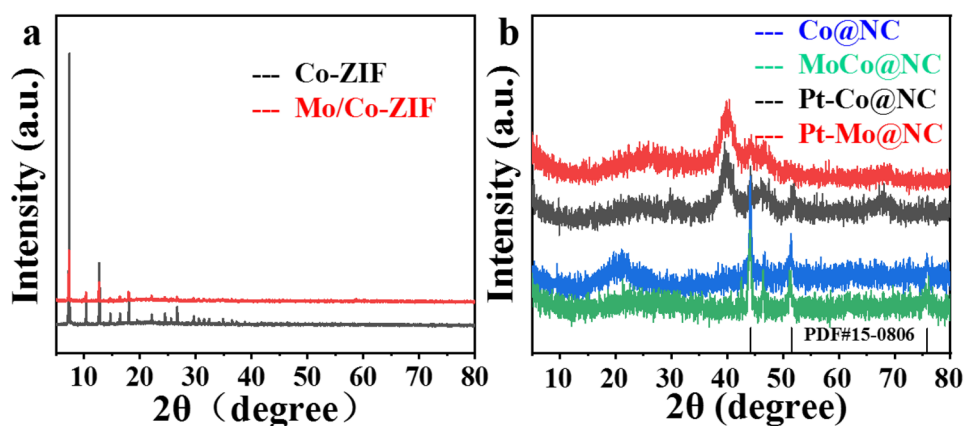
The preparation steps of Pt–Mo/Co@NC nanocomposites are shown in Scheme 1. Firstly, the as-prepared Co-ZIF was dispersed in a methanol solution. Secondly, a moderate ammonium molybdate solution was added and stirred for 1–2 h. During this process, the surface Co^{2+} ions of the Co-ZIF were released into the solution and the molybdate ions in the solution could form coordination bonds with the unetched Co^{2+} to obtain Mo/Co-ZIF composite materials [41]. Then, the Mo/Co-ZIF precursors were calcinated to obtain the Mo/Co@NC composite material. Finally, Pt–Mo/Co@NC nanocomposite material was obtained by a simple microwave-assisted reduction method.

Surface morphology and chemical structure characterization

The XRD pattern of the Co-ZIF and Mo/Co-ZIF is analyzed in Fig. 1a. The XRD diffraction peaks of Co-ZIF polyhedrons suggest the successful preparation of Co-ZIF crystals [31]. Based on the XRD analysis, the peak positions of Mo/Co-ZIF and Co-ZIF were obviously overlapped, but the peak intensity of Mo/Co-ZIF reduced a lot, which shows that the crystal structures of Mo/Co-ZIF and Co-ZIF were basically the same and the decrease of the peak intensity might be due to the separation of Co^{2+} in Co-ZIF. In Fig. 1b, the peak positions of the Mo/Co@NC nanocomposites at 44.2°, 51.4°, and 75.8° corresponded to the (111), (200), and (220) planes of element Co (PDF#15–0806), respectively. Besides, there was a clear peak at around 25°, which corresponded to the (002) plane of derived carbon. Compared with the Co@NC derived from the pure Co-ZIF polyhedron, it could be found that the peak intensity of the Mo/Co@NC was slightly weakened, but the overall crystal structure was the same with Co@NC. Finally, after a small amount of Pt nanoparticles were deposited over Mo/Co@NC surface, XRD analysis of Pt–Mo/Co@NC showed that the 2 θ diffraction peaks at 39.7°, 46.2°, and 67.4° can be matched to the (111), (200), and (220) planes of metallic Pt (PDF#04–0802), respectively. At the same time, the crystal structure of Mo/Co@NC did not change; the decrease of the peak intensity might be attributed to that part of the cobalt was etched away. For comparison, the XRD analysis on Pt–Co@NC was performed, whose crystal structure was consistent with Pt–Mo/Co@NC, which showed that Co@NC was still the foremost composition.

The crystal structures and electronic state for Pt–Mo/Co@NC and Pt–Co@NC were characterized by XPS analysis (Figs. 2 and S1). As revealed in Fig. 2a, the survey spectrum showed Pt–Mo/Co@NC was composed of Mo, Co, N, C, O, and Pt elements. The high-resolution Co 2p spectrum at the binding energies of 778.2, 796.9.0/781.9, and 780.0 eV [38]

Fig. 1 **a** XRD patterns of the Co-ZIF and Mo/Co-ZIF. **b** XRD patterns of Co@NC, Mo/Co@NC, Pt-Co@NC, and Pt-Mo/Co@NC



could be regarded as Co^0 , Co^{2+} , and Co^{3+} (Fig. 2b), and the presence of Co^{2+} and Co^{3+} might be due to the oxidized surface of the metal Co when the sample was exposed to the air. Besides, the peaks at 803.1 and 786.2 eV were the satellite peaks of the metal Co. The Mo 3d spectrum (Fig. 2c) displayed different peaks at 228.6, 229.4, 232.1, and 235.6 eV, manifesting that Mo existed in multiple states, which might be regarded as Mo^{2+} , Mo^{3+} , and Mo^{6+} , respectively. The peaks at 235.6 eV could be regarded as Mo^{6+} from MoO_3 [34]. The presence of MoO_2 and MoO_3 might be caused by partial oxidation on the surface of the molybdenum carbide due to contact with air [61]. As revealed in Fig. 2d, the peaks

of the Pt 4f spectrum for Pt-Mo/Co@NC located at 71.44 and 74.81 eV. Compared with the earlier reports where the peaks of the commercialized Pt/C were located at 71.9 and 75.2 eV [62], the binding energies of our samples decreased, manifesting that Pt obtained many electrons from the Mo/Co@NC carriers, which might be attributed to the electronic effect [14]. On the basis of *d-band* theory, the electrons enriched on the surface of Pt will weaken the occupation of active sites by toxic substances such as CO, thus the catalytic activity of alcohols oxidation was significantly improved compared with the commercially available Pt/C catalyst [3]. In Fig. 2e, the N 1s spectrum exhibited pyridinic-N

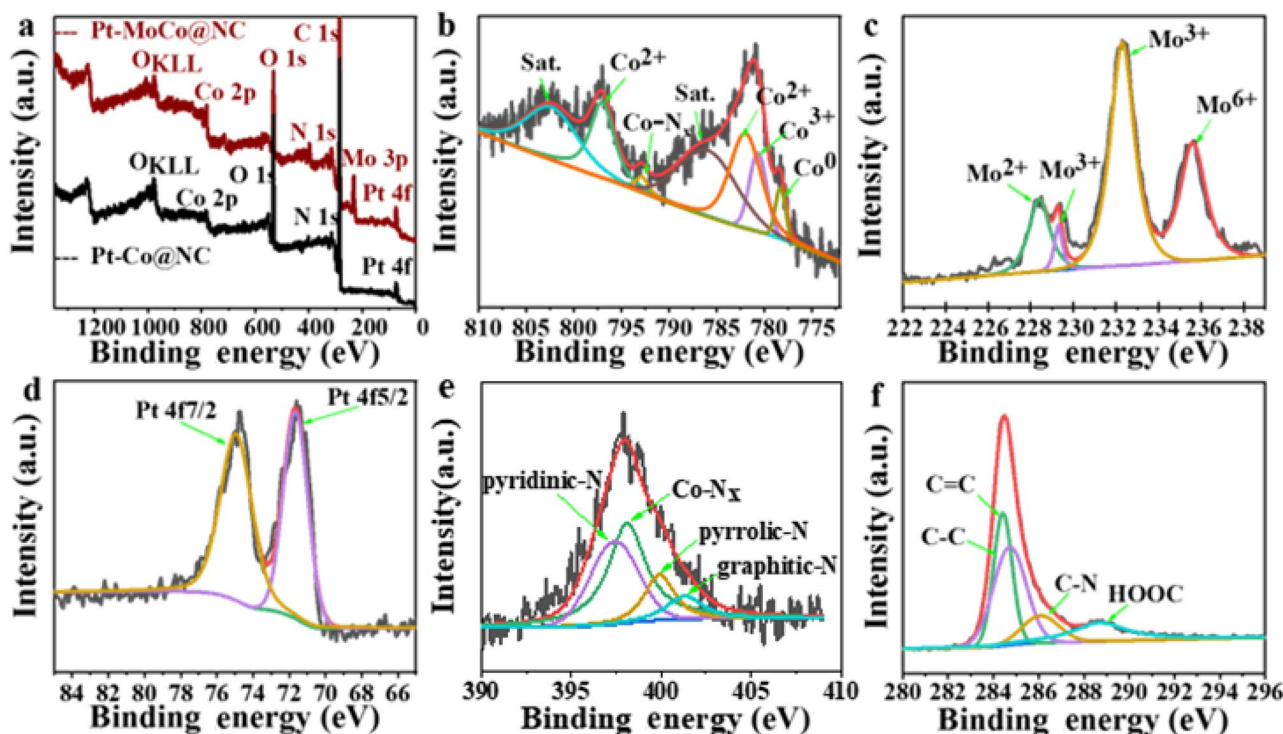


Fig. 2 **a** XPS survey spectrum of Pt-Mo/Co@NC and high-resolution XPS spectra of **b** Co 2p, **c** Mo 3d, **d** Pt 4f, **e** N 1s, and **f** C 1s regions

(397.4 eV), Co-N_x (398.1 eV), pyrrolic-N (399.9 eV), and graphitic-N (401.2 eV). In Fig. 2f, the main peak of the C 1s spectrum is at 284.4 eV as sp² hybridized carbon; other peaks at 285.0, 286.0, and 288.0 eV can be assigned to sp³ hybridized carbon, indicating the existence of C=C, C–C, C–N, and C–O, separately.

FE-SEM was used to analyze the surface morphology of a series of composite materials. In Fig. 3a, the surface of Co-ZIF particles was smooth and polyhedral. After molybdate ion treatment, the surface structure of Mo/Co-ZIF had subtle changes, forming some lamellar structures (Fig. 3d), which also verified that the change of the Mo/Co-ZIF surface structure will cause the decrease of the XRD peak value. As shown in Fig. 3e, after the Mo/Co-ZIF precursor was reduced at a high temperature, the surface of the Mo/Co@NC nanoparticles was coated with a small amount of molybdenum carbide nanoparticles, effectively protecting the inner cobalt nanoparticles from agglomeration and oxidation. As shown in Fig. 3b, there was the Co@NC obtained from the Co-ZIF precursor, which showed a very obvious difference that the Co nanoparticles derived from the Co-ZIF had a very obvious agglomeration without the protection of molybdenum particles. Finally, the morphology analysis of Pt–Mo/Co@NC showed that the surface of Mo/Co@NC was loaded with a small amount of Pt nanoparticles, which was consistent with our expected results (Fig. 3f). Similarly, the topography analysis of the Pt–Co@NC also showed a similar surface structure (Fig. 3c). N₂ adsorption–desorption isotherms for the Mo/Co@NC and

Co@NC are shown in Fig. S7. The specific surface areas of Mo/Co/@NC and Co@NC are 242.68 m² g^{−1} and 107.99 m² g^{−1}, respectively, indicating that the doping of molybdenum has significantly increased the surface area.

The architecture and the distribution of the compound of the Pt–Co@NC and Pt–Mo/Co@NC composites were further evaluated by TEM, HRTEM, and EDX elemental mapping (Figs. S2 and 4). Firstly, the TEM tests of the Pt–Mo/Co@NC composite (Fig. 4a, b) revealed a clear three-dimensional frame structure. At the same time, after statistical analysis, Pt nanocrystals with a mean particle size of 2.0 ± 1 nm were shown uniformly distributed in Fig. 4b. Such a surprising result might be attributed to the interface effect of metal–carbon support [14]. In Fig. 4c–e, the HRTEM image showed three clear lattice fringes with a spacing distance of 0.23 nm, 0.2 nm, and 0.34 nm, corresponding to Pt (111) plane, Co (111) plane, and C (002) plane, separately, which was consistent with the result of XRD analysis. In addition, as shown in Fig. 4f, the interplanar crystal spacing of 0.24 nm reflects the (002) plane of Mo, which implied that there was molybdenum carbide in composite materials. The SAED pattern analysis (Fig. 4g) also showed results consistent with the HR-TEM.

Elemental mapping images of Pt–Mo/Co@NC are shown in Fig. 5b–f. Pt, Co, Mo, N, and C manifested a uniform distribution, and it was consistent with the results of the TEM lattice pattern. In addition, the SEM EDX spectrum analysis of Pt–Mo/Co@NC and Pt–Co@NC showed that the quality ratio of Pt in the composite material was about 6.5 wt% (Fig. S3a,

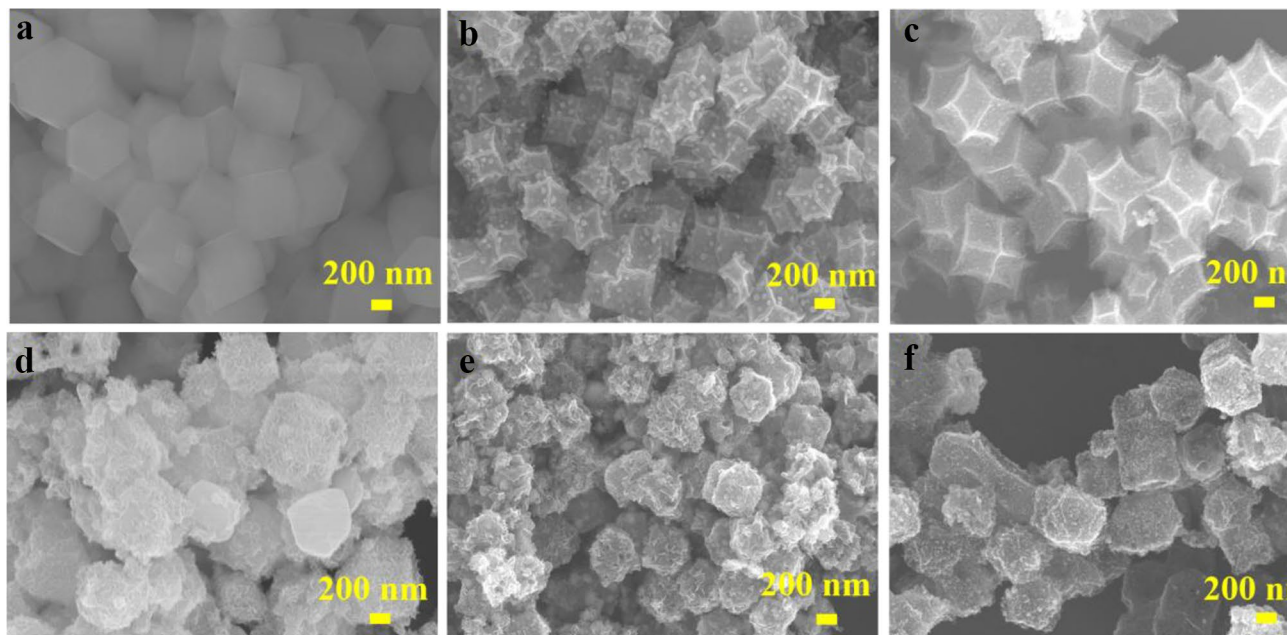
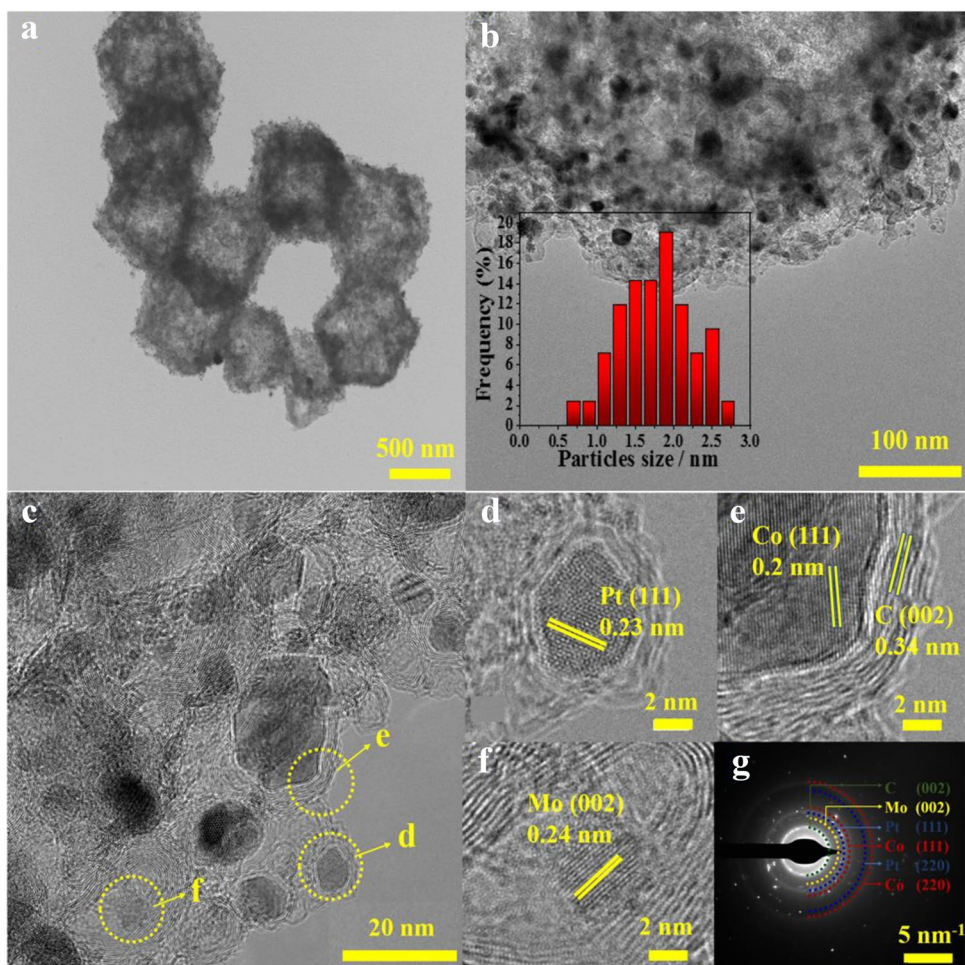


Fig. 3 a SEM images of the Co-ZIF, b SEM images of the Co@NC, c SEM images of the Pt–Co@NC, d SEM images of the Mo/Co-ZIF, e SEM images of the Mo/Co@NC, f SEM images of the Pt–Mo/Co@NC

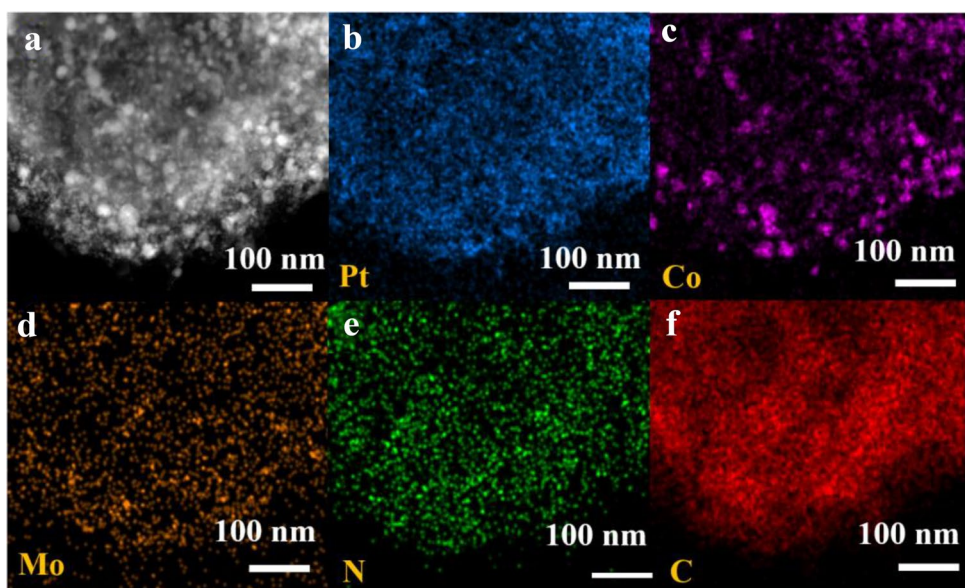
Fig. 4 **a,b** TEM images of the Pt–Mo/Co@NC, the inset of **b** is the particle size distribution histogram of Pt nanoparticles in the Pt–Mo/Co@NC. **c–g** HR-TEM images and SAED pattern of Pt–Mo/Co@NC



b), which was consistent with our expectation. According to the interface effect of the metal carrier, a small amount of Pt nanocrystals could be grown on the Mo/Co@NC surface by a

simple microwave-assisted reduction. In Fig. S4, the elemental mapping images of the Pt–Co@NC are shown, which also exhibited a uniform distribution of Pt, Co, N, and C.

Fig. 5 **a–f** Elemental mapping images of Pt–Mo/Co@NC



Electrochemical performance characterization

The MOR activities of different composite materials were evaluated by cyclic voltammetry (CV). The cyclic voltammograms of the Pt–Mo/Co@NC and Pt–Co@NC catalysts in 1 M KOH at a potential scan rate of are shown in Fig. S8. For the Pt–Mo/Co@NC catalyst, however, a noticeable increase in the double-layer capacitance is observed that may be attributed to the formation of oxygenated molybdenum species on the surface.

The CV analysis of Co-ZIF, Mo/Co-ZIF, Co@NC, and Mo/Co@NC was performed in a 1 M KOH + 1 M methanol solution with a potential range of $-0.5 \sim 0.5$ V at a scan rate of 50 mV/s for 10 cycles. As could be distinctly seen in Fig. 6a, c, this series of non-noble metal catalysts exhibited a certain catalytic activity, and the highest specific activity and mass activity of the Mo/Co@NC had a peak current of 50 mA cm^{-2} and 883 mA mg^{-1} , separately. The result corresponded to the previous series of characterizations, and the doping of molybdenum had greatly improved the catalytic activity of methanol. As indicated in Fig. 6b, d, Pt–Mo/Co@NC exhibited the highest mass activity and area activity, reaching 1727 mA mg^{-1} and 98 mA cm^{-2} in the potential range of $-0.1 \sim 0.5$ V, respectively. It was around 1.9 and 2.2 times of Mo/Co@NC and Pt–Co@NC, respectively, compared with the peak efficiency of the as-prepared catalyst shown in Fig. 7a, b. In Fig. S6a, MOR curves of the Pt–Mo/Co@NC before and after 10,000 cycles show that the peak mass density drops from 1727 to 1167 mA mg^{-1} , reducing of efficiency by 30%, which is normal for our as-prepared catalyst and proves that the Pt–Mo/Co@NC

catalyst has preferable stability. Regarding the comparison of catalyst performance, in Table S1, the Pt–Mo/Co@NC was compared with the Pt/C catalyst and the other catalysts. The mass catalytic activity of Pt–Mo/Co@NC was about 4.3 times improved by the commercially available Pt/C catalyst, indicating the superior anti-CO poisoning effect of Pt–Mo/Co@NC. In addition, the active sites of the Pt–Mo/Co@NC catalyst are mainly Pt nanoparticles, Mo_2C on the surface, and Co on the inner layer. The improvement of the as-prepared catalyst activity and stability was mainly because of the following factors: (a) the interface effect of the metal carrier made Pt nanoparticles gain more electrons, which reduced the CO poisoning effect, increasing the catalytic activity and stability; (b) the multi-metal synergistic effect of the metal carrier Mo/Co@NC with certain catalytic activity and Pt nanoparticles promoted the methanol oxidation reaction; (c) Mo/Co@NC with a three-dimensional structure provided sufficient attachment sites for Pt nanoparticles, making Pt nanoparticles have excellent dispersion and uniformity; and (d) the doping of high-valence Mo regulated the crystalline and electronic structures of the catalyst, which increased the catalytic sites and accelerated the electron transport, thus improving the electrocatalytic performance of MOR[63].

To further verify the CO tolerance of the catalyst, CO-stripping voltammetry was performed in a 1 M KOH solution (Fig. S9). Compared with Pt–Co@NC (-0.296 V), the peak potential of Pt–Mo/Co@NC (-0.4754 V) is more negative; that is, the CO oxidation potential is more negative, indicating that Pt–Mo/Co@NC is easier to oxidize CO at a lower potential. This is consistent with the

Fig. 6 a,c Cyclic voltammograms curves for MOR catalyzed by Co-ZIF, Mo/Co-ZIF, Co@NC, Mo/Co@NC. b,d Cyclic voltammograms curves for MOR catalyzed by Pt–Co@NC and Pt–Mo/Co@NC. The CVs were obtained at a scan rate of 50 mV s^{-1} in an alkaline solution of 1.0 M KOH and 1.0 M CH_3OH

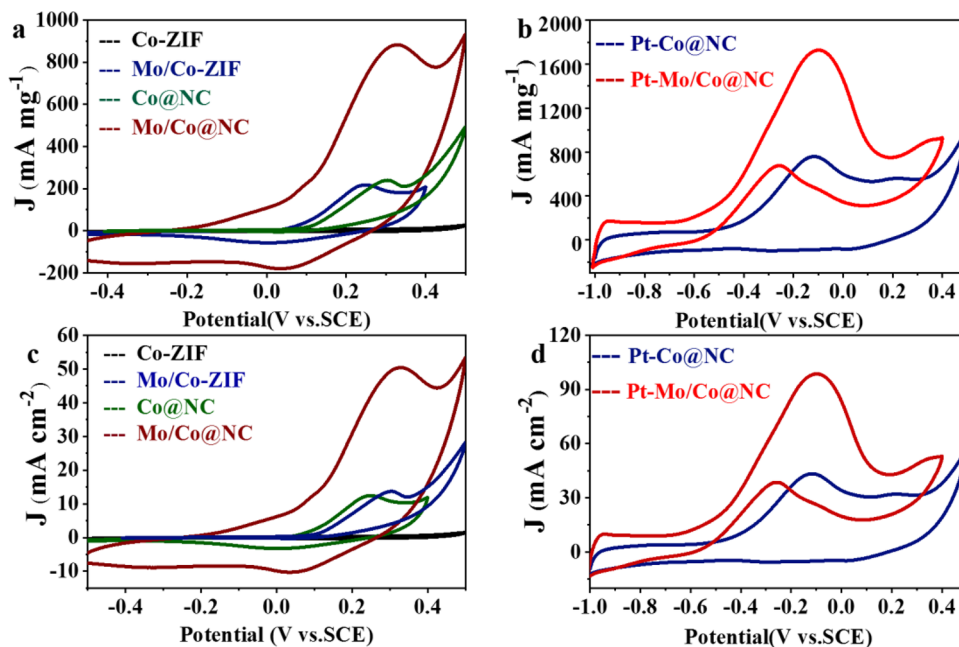
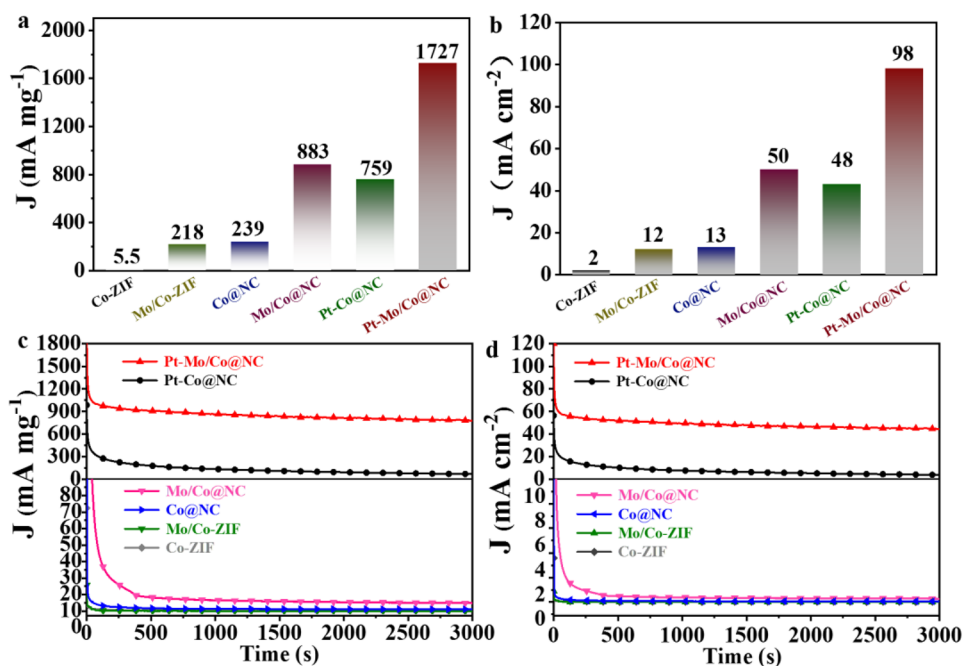


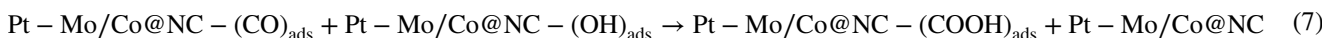
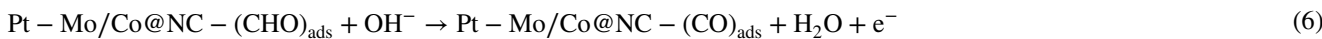
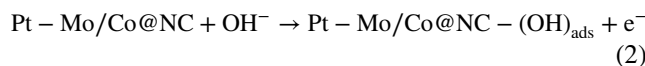
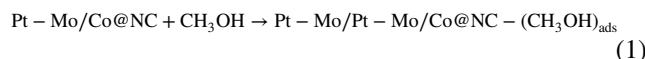
Fig. 7 **a–b** Mass activity and specific activity of the as-prepared catalysts for methanol oxidation. **c–d** Chronoamperometric curve for MOR catalyzed by the Co-ZIF, Mo/Co-ZIF, Co@NC, Mo/Co@NC, Pt-Co@NC, and Pt-Mo/Co@NC at 0.3 V vs in 1.0 M KOH and 1.0 M CH₃OH



previous results and further demonstrates that Pt-Mo/Co@NC has better CO tolerance.

The stability of our catalysts was measured by chronoamperometry (CA). The stability measurements of Co-ZIF, Mo/Co-ZIF, Co@NC, and Mo/Co@NC were carried out at 0.3 V vs. SCE for 3000 s; the Pt-Mo/Co@NC and Pt-Co@NC were carried out at -0.1 V vs. SCE for 3000 s. As shown in Fig. 7c and d, for all catalysts, the curve began with an ultra-rapid descent and then gradually reached an approximate steady state. In Fig. S5b, the chronoamperometric curves of the Pt-Mo/Co@NC show that the attenuation of Pt-Mo/Co@NC was smaller than 20% Pt/C, indicating that, although the Pt content of as-prepared Pt-Mo/Co@NC was only 6.5%, its stability was much higher than 20% Pt/C. However, the decay rate of

the Pt-Mo/Co@NC electrode was much slower than other catalysts, and according to the interface effect of the metal carrier [62, 64], there were abundant electrons around Pt nanoparticles when they deposited over the Mo/Co@NC surface, which could weaken the ability of adsorption of CO-poisoning species. Thus, the catalytic stability of the Pt-Mo/Co@NC was better than other as-prepared catalysts. The electron transfer mechanism of the Pt-Mo/Co@NC catalyst surface in alkaline media during MOR probably abides by the steps below [65, 66]:





These MOF-derived nanocomposites have great performances as valid electrocatalysts for DMFC. Firstly, a single metal Co-ZIF was prepared. Then, a molybdate precursor containing Mo metal was adsorbed on the surface and pores of Co-ZIF. After pyrolyzed at an appropriate temperature and atmosphere, the cobalt@nitrogen-doped carbon nanocomposites with a small amount of molybdenum carbide (marked as Mo/Co@NC) were prepared, and it was often referred to as an armor catalyst. The molybdenum carbide on the surface provided a protective coat of armor for the cobalt elements in the inner layer. The strong coupling effect between the metal and the carrier not only makes the molybdenum carbide have a certain methanol oxidation performance but also provides abundant electrons for the surface Pt nanoparticles.

Conclusions

A small amount of Pt nanoparticles (6.5%) were deposited over Mo/Co@NC surface by microwave-assisted method, then a small amount of Pt modified Mo/Co@NC composite material was obtained. A great deal of electrons would accumulate around the Pt nanoparticles on the surface of Mo/Co@NC via the strong interaction between the metal and the metallic carbon carrier, which greatly reduced the CO poisoning effect, improving catalytic activity and stability. In this method, non-noble metals and platinum nanocrystals were ingeniously combined, effectively solving the problems of low stability of non-noble metal catalysts and the high cost of platinum catalysts, which provide a good idea for the synthesis of low platinum content catalysts.

Supplementary Information The online version contains supplementary material available at <https://doi.org/10.1007/s10008-022-05311-x>.

Declarations

Competing interests The authors declare no competing interests.

References

- Gong LY, Yang ZY, Li K, Xing W, Liu CP, Ge JJ (2018) *J Energy Chem* 27:1618–1628
- Xia ZX, Zhang XM, Sun H, Wang SL, Sun GQ (2019) *Nano Energy* 65:104048
- Monyoncho EA, Ntais S, Brazeau N, Wu J-J, Sun C-L, Baranova EA (2016) *ChemElectroChem* 3:218–227
- Liu MM, Zhang RZ, Chen W (2014) *Chem Rev* 114:5117–5160
- Debe MK (2012) *Nature* 486:43–51
- Peng K, Zhang WQ, Bhuvanendran N, Ma Q, Xu Q, Xing L, Khotseng L, Su HN (2021) *J Colloid Interface Sci* 598:126–135
- Lei FL, Li ZS, Zhang L, Wang YL, Xu SH, Lin S (2016) *J Electrochem Soc* 163:F913–F918
- Abdullah RM, Kamarudin SK, Loh KS (2018) *Int J Hydrogen Energy* 03603199
- Qiao Y, Liu YF, Liu Y, Dong Q, Zhong G, Wang X, Liu ZY, Wang XZ, He SM, Zhou WQ, Wang GF, Wang C, Hu LB (2020) *Small methods* 4:2000265
- Zhang S, Zeng ZC, Li QQ, Huang BL, Zhang XY, Du YP, Yan C-H (2021) *Energy Environ Sci* 14:5911–5918
- Pezeshkvar T, Norouzi B, Moradian M, Mirabi A (2022) *J Solid State Electr* 26:1479–1492
- Xia ZX, Xu XL, Zhang XM, Li HQ, Wang SL, Sun GQ (2020) *J Mater Chem A* 8:1113–1119
- Liao YX, Li J, Zhang SM, Chen SL (2021) *Chin J Catal* 42:1108–1116
- Willinger E, Tarasov A, Blume R, Rinaldi A, Timpe O, Massue C, Scherzer M, Noack J, Schlögl R, Willinger MG (2017) *ACS Catal* 7:4395–4407
- Wang YJ, Du CY, Sun YP, Han GK, Kong FP, Yin GP, Gao YZ, Song Y (2017) *Electrochim Acta* 254:36–43
- Kakati N, Maiti J, Lee SH, Jee SH, Viswanathan B, Yoon YS (2014) *Chem Rev* 114:12397–12429
- Huang L, Wei M, Hu N, Tsiakaras P, Shen PK (2019) *Appl Catal B Environ* 258:117974
- Gong WH, Jiang Z, Wu RF, Liu Y, Huang L, Hu N, Tsiakaras P, Shen PK (2019) *Appl Catal B Environ* 246:277–283
- Chang JF, Feng LG, Jiang K, Xue HG, Cai W-B, Liu CP, Xing W (2016) *J Mater Chem A* 4:18607–18613
- Tian H, Yu YH, Wang Q, Li J, Rao P, Li RS, Du YL, Jia CM, Luo JM, Deng PL, Shen YJ, Tian XL (2021) *Int J Hydrogen Energy* 46:31202–31215
- Gawande MB, Goswami A, Asefa T, Guo HZ, Biradar AV, Peng D-L, Zboril R, Varma RS (2015) *Chem Soc Rev* 44:7540–7590
- Zhang J, Wang RY, Hu XQ, Sun ZP, Wang XC, Guo Y, Yang LL, Lou MR, Wen PT (2020) *Appl Surf Sci* 533:147319
- Wei Y, Zhang X, Liu YJ, Jia CC, Yang P (2020) *Electrochim Acta* 349:136366
- Li XL, Liu Y, Zhu JL, Tsiakaras P, Shen PK (2022) *J Colloid Interface Sci* 607:1411–1423
- Kocak CC, Dursun Z (2022) *Mater Sci Eng B* 275:115485
- Rivera-Gonzalez H, Torres-Pacheco L, Alvarez-Contreras L, Olivas A, Guerra-Balcazar M, Valdez R, Arjona N (2019) *J Electroanal Chem* 835:301–312
- Miura K, Watanabe R, Fukuhara C (2020) *Surf Sci* 696:121601
- Zhu ZJ, Chen CM, Cai MQ, Cai Y, Ju HX, Hu SW, Zhang M (2019) *Mater Res Bull* 114:161–169
- Wang QC, Wang ZH, Liang XL, An SL, Cai CK, Liu YY, Bao JX, Song XW (2021) *J Electrochem Soc* 168:052507
- Karki SB, Hona RK, Ramezanipour F (2022) *J Solid State Electr* 26:1303–1311
- Xin W-L, Lu K-K, Shan D (2019) *Appl Surf Sci* 481:313–318
- Alharbi FF, Nisa MU, Hassan HMA, Manzoor S, Ahmad Z, Abid AG, Aman S, Ashiq MN, El-Nasser KS, Taha TAM (2022) *J Solid State Electr* 26:2171–2182
- Asen P, Haghighi M, Shahrokhian S, Taghavinia N (2019) *J Alloys Compd* 782:38–50
- Yu F, Chen ZH, Guo ZZ, Irshad MS, Yu L, Qian JW, Mei T, Wang XB (2020) *ACS Sustainable Chem Eng* 8:7139–7149
- Xia ZH, An L, Chen PK, Xia DG (2016) *Adv Energy Mater* 6:1600458

36. Shah SSA, Najam T, Aslam MK, Ashfaq M, Rahman MM, Wang K, Tsiakaras P, Song SQ, Wang Y (2020) *Appl Catal B Environ* 268:118570
37. Lv YH, Li XW (2020) *Int J Hydrogen Energy* 45:12766–12776
38. Gao QS, Zhang WB, Shi ZP, Yang LC, Tang Y (2019) *Adv Mater* 31:1802880
39. Abrego-Martinez JC, Wang YL, Moreno-Zuria A, Wei QL, Cuevas-Muniz FM, Arriaga LG, Sun SH, Mohamedi M (2019) *Electrochim Acta* 297:230–239
40. Zhang K, Zhang G, Qu JH, Liu HJ (2018) *ACS Appl Mater Interfaces* 10:2451–2459
41. Wu C, Liu D, Li H, Li JH (2018) *Small* 14:1704227
42. Wang YQ, Tao L, Xiao ZH, Chen R, Jiang ZQ, Wang SY (2018) *Adv Funct Mater* 28:1705356
43. Maduraiveeran G, Sasidharan M, Jin W (2019) *Prog Mater Sci* 106:100574
44. Fagiolari L, Varaia E, Mariotti N, Bonomo M, Barolo C, Bella F (2021) *Adv Sust Syst* 5:2100025
45. Rahman NA, Hanifah SA, Mobarak NN, Ahmad A, Ludin NA, Bella F, Su'ait MS (2021) *Polymer* 230:124092
46. Amici J, Torchio C, Versaci D, Dessantis D, Marchisio A, Caldera F, Bella F, Francia C, Bodoardo S (2021) *Polymers* 13:1625
47. Alidoost M, Mangini A, Caldera F, Anceschi A, Amici J, Versaci D, Fagiolari L, Trotta F, Francia C, Bella F, Bodoardo S (2022) *Chem Eur J* 28:e202104201
48. Reina M, Scalia A, Auxilia G, Fontana M, Bella F, Ferrero S, Lamberti A (2022) *Adv Sust Syst* 6:2100228
49. Abdah MAAM, Mokhtar M, Khoon LT, Sopian K, Dzulkurnain NA, Ahmad A, Sulaiman Y, Bella F (2021) *Su'ait MS. Energy Rep* 7:8677–8687
50. Liang ZZ, Zhang CC, Yuan HT, Zhang W, Zheng HQ, Cao R (2018) *Chem Commun* 54:7519–7522
51. Zhang H, Liu XM, Wu Y, Guan C, Cheetham AK, Wang J (2018) *Chem Commun* 54:5268–5288
52. Lu XF, Xia BY, Zang S-Q, Lou XW (2020) *Angew Chem Int Ed* 59:4634–4650
53. Liu QY, Li ZK, Wang DH, Li ZF, Peng XL, Liu CB, Zheng PL (2020) *Front Chem* 8:694
54. Bai X-J, Chen H, Li Y-N, Shao L, Ma J-C, Li L-L, Chen J-Y, Wang T-Q, Zhang X-M, Zhang L-Y, Fu Y, Qi W (2020) *New J Chem* 44:1694–1698
55. Huang W, Tang J, Diao FY, Engelbrekt C, Ulstrup J, Xiao XX, Molhave K (2020) *ChemElectroChem* 7:4695–4712
56. Yang WP, Li XX, Li Y, Zhu RM, Pang H (2019) *Adv Mater* 31:1804740
57. Zhu XY, Wang J, Chai LL, Tang GS, Wan KN, Pan JQ (2022) *J Solid State Electr* 26:1163–1173
58. Troyano J, Carne-Sanchez A, Avci C, Imaz I, MasPOCH D (2019) *Chem Soc Rev* 48:5534–5546
59. Wei Y-S, Zhang M, Zou RQ, Xu Q (2020) *Chem Rev* 120:12089–12174
60. Zhan W, Ma L, Gan MY, Ding JJ, Han SC, Wei DY, Shen J, Zhou CL (2020) *Int J Hydrogen Energy* 45:15630–15641
61. Chen Y-Y, Zhang Y, Jiang W-J, Zhang X, Dai ZH, Wan L-J, Hu J-S (2016) *ACS Nano* 10:8851–8860
62. Wang FL, Fang B, Yu X, Feng LG (2019) *ACS Appl Mater Interfaces* 11:9496–9503
63. Li LQ, Gao W, Tang KW, Lei M, Yao B, Qi WH, Wen D (2021) *Electrochim Acta* 369:137692
64. Upadhyay S, Pandey OP (2022) *J Solid State Electr* 26:559–564
65. Housmans THM, Wonders AH, Koper MTM (2006) *J Phys Chem B* 110:10021–10031
66. Cao D, Lu G-Q, Wieckowski A, Wasileski SA, Neurock M (2005) *J Phys Chem B* 109:11622–11633

Publisher's Note Springer Nature remains neutral with regard to jurisdictional claims in published maps and institutional affiliations.

Springer Nature or its licensor (e.g. a society or other partner) holds exclusive rights to this article under a publishing agreement with the author(s) or other rightsholder(s); author self-archiving of the accepted manuscript version of this article is solely governed by the terms of such publishing agreement and applicable law.